Chapter 26 – NUMERICAL SOLUTIONS FOR THE VFE-2 CONFIGURATION ON STRUCTURED GRIDS AT ONERA, FRANCE

by

Jean-François Le Roy and Jacques Riou

26.1 INTRODUCTION

The flow over delta wings is the place of numerous vortical phenomena. The flow separates at leading edge for lower incidence in the case of a sharp leading edge than for a rounded leading edge. Separation generates a mixing layer leading to a primary vortex on the upper side of the wing. According to the value of the angle of attack and the wing shape, a secondary vortex or even a tertiary one can be observed. These vortices contribute for a large part to the lift (vortical lift). At high angle of attack the primary vortex breakdown occurs, what strongly alters the flow. This phenomenon is characterised by a sudden expansion of the vortical core and a rapid drop of the axial velocity. This leads to large variations of lift, drag and roll coefficients because the vortices become unstable, yielding to asymmetric oscillations [[26-1], [26-2]]. The lift coefficient is then highly correlated to the longitudinal location of the vortex breakdown. The breakdown negative effects appear not only through the average performance, but also because the essential unsteady nature of the flow generates buffet and loss of control. Accurate CFD simulations of these types of flow will help the designer and will also allow assessing efficient control means of large scale vortical structures.

In the following sections, steady and unsteady approaches are presented. General description of the methods, meshes, turbulence models and boundary conditions are described. The results of the simulations are compared with experimental data to validate the numerical approach. Finally, a conclusion is given to exhibit the ability of CFD methods to predict such flows.

26.2 NOMENCLATURE

U_0, U_∞	freestream velocity, m/s
u, v, w	velocity components, m/s
Ωx	x vorticity component, = (dw/dy – dv/dz)
St_c	Strouhal number, based on the root chord
$\frac{f.G(f)}{\sigma^2}$	Power Spectral Density

26.3 STEADY APPROACH

All the steady simulations have been done with the ONERA elsA software (standing for Ensemble Logiciel pour la Simulation en Aérodynamique). The elsA software solves the compressible, three-dimensional Reynolds average Navier-Stokes equations in a cell centered finite-volume formulation from low subsonic to high supersonic velocities [[26-3], [26-4]].

26.3.1 Computational Grids

The configurations considered in this study are the NASA 65 degrees delta wing with a sharp and a medium leading edges. The recommended computational domain sets the outer boundary at 10 Root Chord (c_r) upstream from wing apex, 20 c_r downstream from wing apex, 20 c_r above wing apex, 20 c_r under wing apex and 10 c_r spanwise from wing center-line.

In a first step, our own grids have been built around the two geometries with the ICEM Hexa meshing tool. These structured grids have an H-H topology to fit between the model at zero incidence and the far field and a O topology around the sting, Figure 26-1 (a). The wing is described by 165 points along the x direction and 93 points in the spanwise direction. Preliminaries computations allowed to set a local refinement in the upper blocks in order to better resolve the separated region, Figure 26-1 (b). The wing is then described by 281 points in the upper block and 165 points in the lower block along the x direction and 97 points in the spanwise direction.

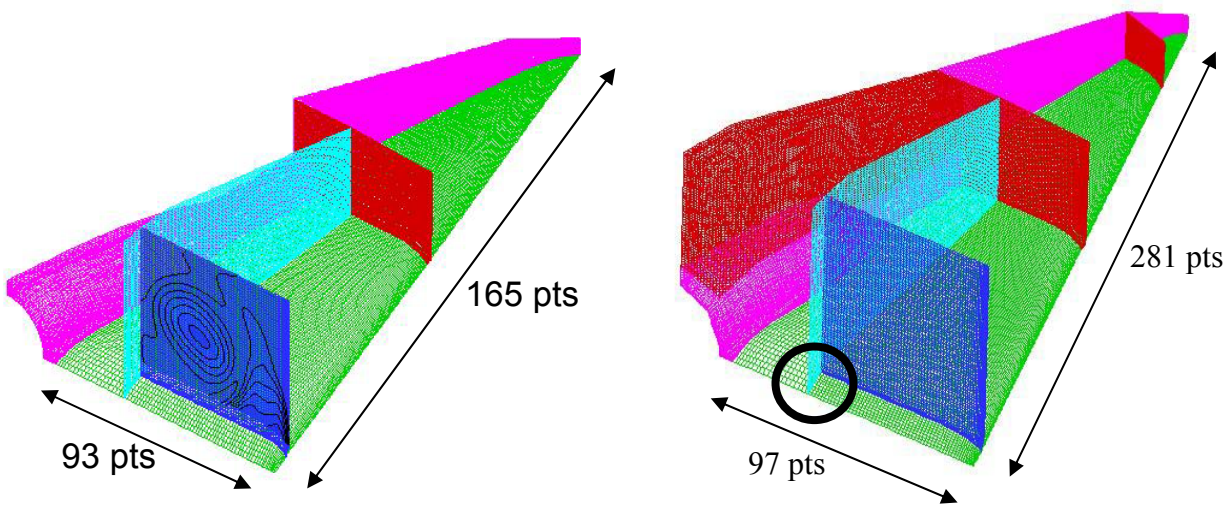

(a) Original Grid **(b) Patched Grid**

Figure 26-1: Structured Grids.

In a second step, common grids generated by W. Fritz from EADS-M Germany have been used to complete the comparisons [26-5]. These two kinds of grid are noted PG for patched grid and CG for common grid.

26.3.2 Computational Method

The set of ordinary differential equations in time is solved by means of the implicit backward Euler scheme. The resolution of the turbulence equations are not coupled to the others and the Harten's parameter is set equal to a small value (0.05) in order to achieve the needed accuracy. The 2nd order scheme of Jameson is used to compute the convective fluxes. The combination of the latest with the backward Euler resolution ensures a sufficient robustness. Due to the fact that only the steady state is of interest the different equations are solved by a local time stepping approach based on the maximum allowable time step for each cell in the current

investigations (CFL = 5.0). Since the convergence speed-up is an important issue, a multi-grid technique has been used to improve the convergence rates: 2 levels with a V cycle and two sub-iterations on the coarse grid.

Different turbulence models have been used. At low angle of attack when the flow is attached the Wilcox k-ω turbulence model is preferred. At higher incidence when the flow is massively separated the Spalart-Allmaras turbulence model with rotational correction (SARC) is better adapted.

26.3.3 Aerodynamic Conditions

Computations have been performed as closely as possible to experimental conditions. The Mach numbers range from 0.2 to 0.4. As a result, the associated Reynolds numbers based on the root chord of the model are in the order of 2 to 6 millions.

Three interesting incidences have been selected for the computations: $\alpha = 13$, 19 and 23°. While at an incidence of 13° the flow remains attached for the 'medium' leading edge, it is separated for the 'sharp' leading edge. At 19° of incidence, the vortex breakdown appears close to the trailing edge and at 23°, the vortex breakdown should be located in the vicinity of the mid chord.

Initial conditions are those of the uniform flow.

A single processor NEC SX-8R (2.2 GHz) has been used for the RANS simulations. The 'patched grid' associated with the SARC model requires a memory of 3900 Mo and the 'common grid' associated with the same model requires 8100 Mo.

26.3.4 Sharp Leading Edge Results

The flow behaviour is analysed from the streamlines and the pressure distributions on the wing surface, the axial vorticity or total pressure losses in some planes and 3D visualizations. Comparisons between our simulations and Luckring's database [26-6] are mainly performed on the pressure distributions.

At an incidence of 13° the surface pressure distribution shown in Figure 26-2 (a) illustrates the separation of the flow along the leading edge. The fluctuations of pressure between the primary vortex and the leading edge indicate that a secondary vortex takes place around the mid chord. This phenomenon is only simulated with the Patched Grid, showing that the grid refinement is important.

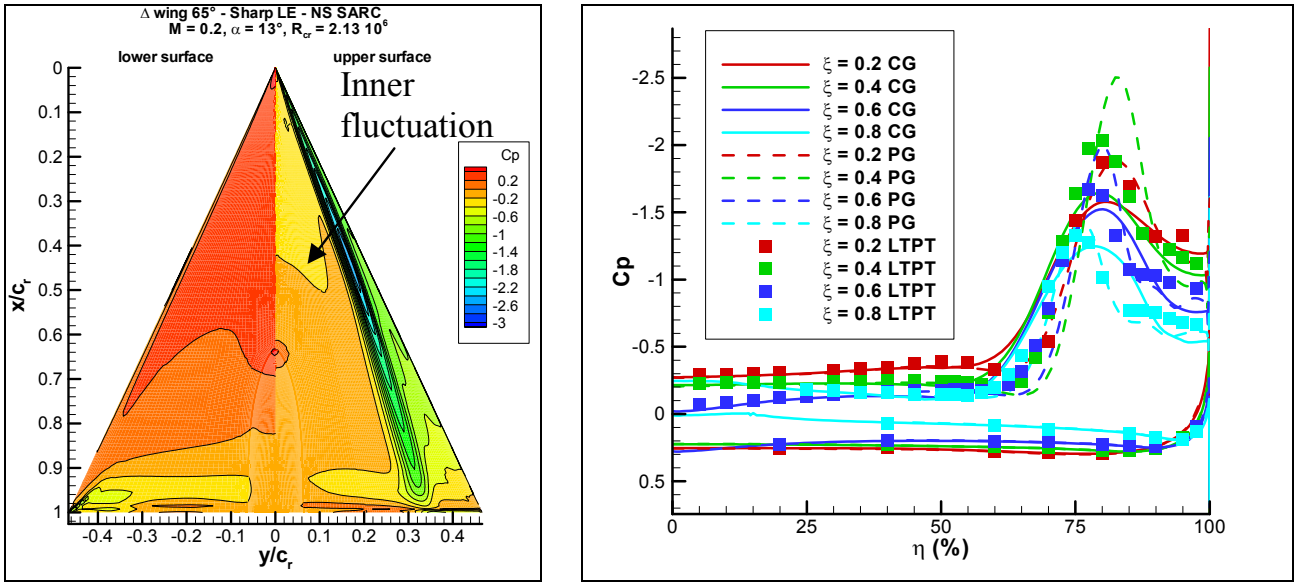

(a) Surface Pressure Distribution for PG **(b) Comparison CFD Results and LTPT Data**

Figure 26-2: Sharp Leading Edge Results – α = 13°.

A comparison between the results obtained with the different grids at the same aerodynamic conditions and LTPT data is plotted in Figure 26-2 (b). The common grid (CG) provides an expanded weak primary vortex. The patched grid (PG) pressure distribution seems to be in a better accordance with the experimental values. Nevertheless at the second station ($\xi = 0.4$) the suction peak is over estimated. The flow along the vortex axis accelerates up to the second station but it is not so intense in the experiments. A very small variation of pressure, noted as 'inner fluctuation' is visible on surface pressure distribution. This fluctuation is also observed in the inner part at the first station. This vanished phenomenon is inherent to the type of leading edge and it will be shown in the following that the same phenomenon can be observed for the 'medium' leading edge with an amplified intensity, emerging then as an additional inner vortical structure.

At 19° of incidence, Figure 26-3 (a) indicates that the primary vortex becomes stronger. The axial vorticity increases with the incidence along the leading edge and in the vortex core. The fluctuations of pressure observed between the primary vortex and the leading edge indicate the presence of a secondary vortex. The secondary vortex is developed all along the primary vortex. The phenomenon is clearly visible for all results at each station. The pressure distributions obtained with the different grids are in better accordance in this configuration. The secondary vortex onset moves upstream towards the apex as incidence increases. An analysis of velocity field shows that the vortex breakdown is located close to the trailing edge at $x/c_r = 0.89$.

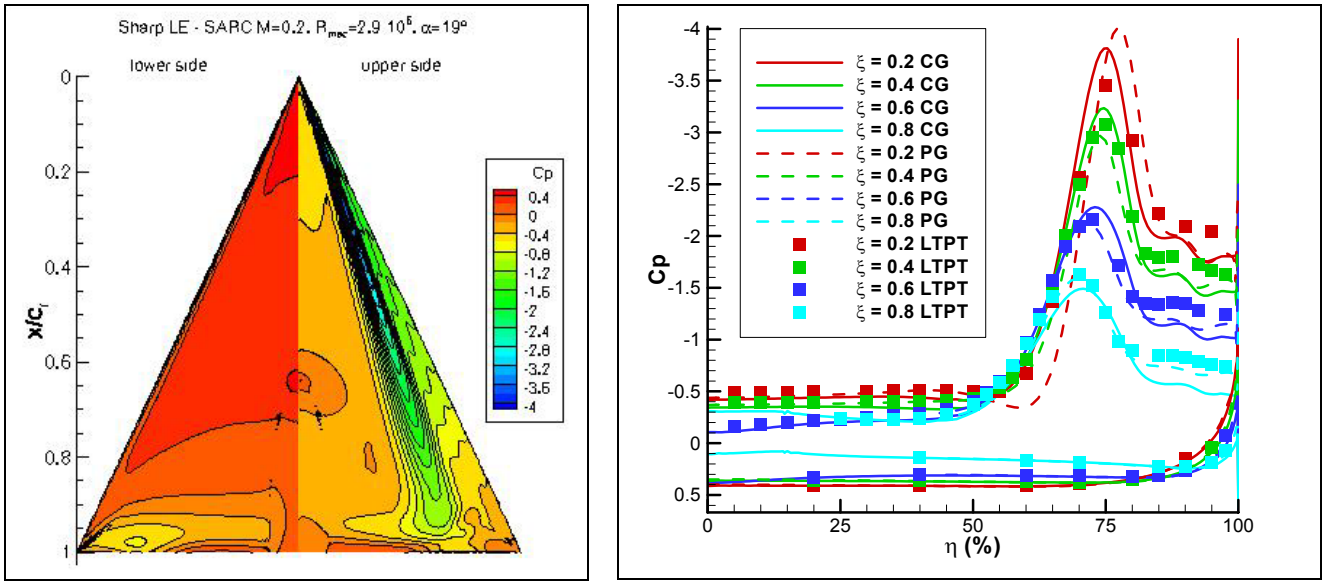

(a) Surface Pressure Distribution for CG **(b) Comparison CFD Results / LTPT Data**

Figure 26-3: Sharp Leading Edge Results – α = 19°.

For a higher incidence (23°), the intensity of the suction peak keeps on rising up (Figure 26-4 (a)). The analysis of the velocity field shows that the vortex breakdown is located at $x/c_r = 0.82$ for the common grid and 0.75 for the patched grid, Figure 26-4 (b). The location of the primary vortex breakdown moves upstream as the incidence increases. Figure 26-5 (a) shows the axial velocity distribution in a plane parallel to the wing at $\Delta z/c_r = 0.0034$. The primary vortex is not visible in this plane but it is marked by a dashed line. The secondary vortex core is not very intense before the emergence of a negative velocity area. The secondary vortex breakdowns in the rear part of the wing ($x/c_r = 0.9$). The streamlines are plotted in Figure 26-5 (b). The secondary vortex breakdown pointed out in the previous figure generates a reverse flow above the rear part of the wing between the attachment and the separation lines.

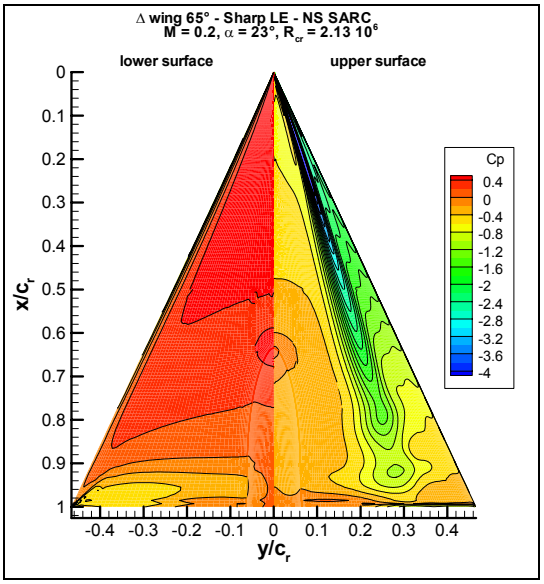

(a) Surface Pressure Distribution

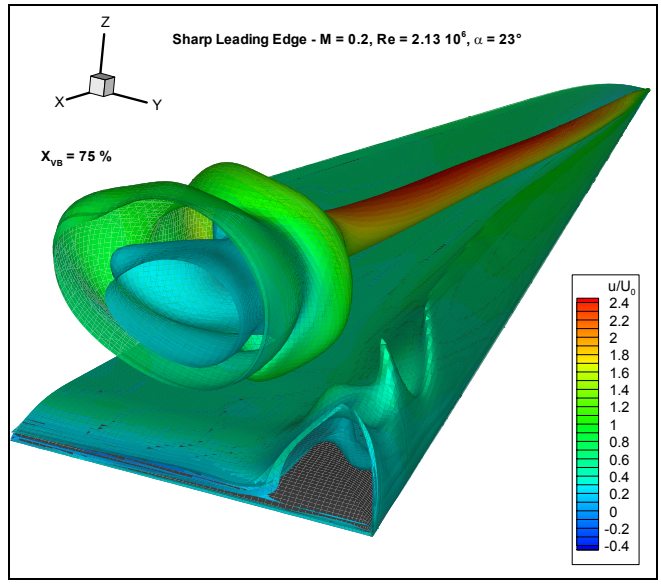

(b) Visualization of the Vortex Breakdown

Figure 26-4: Sharp Leading Edge Results for PG – α = 23°.

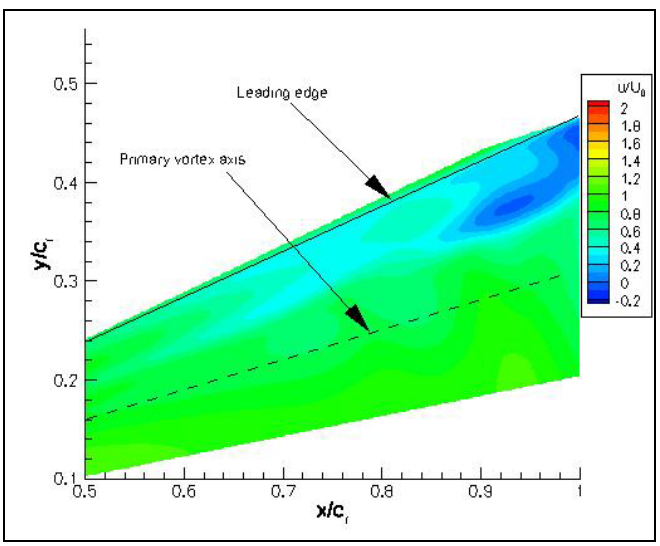

(a) Parallel Plane $\Delta z/c_r$ = 0.0035

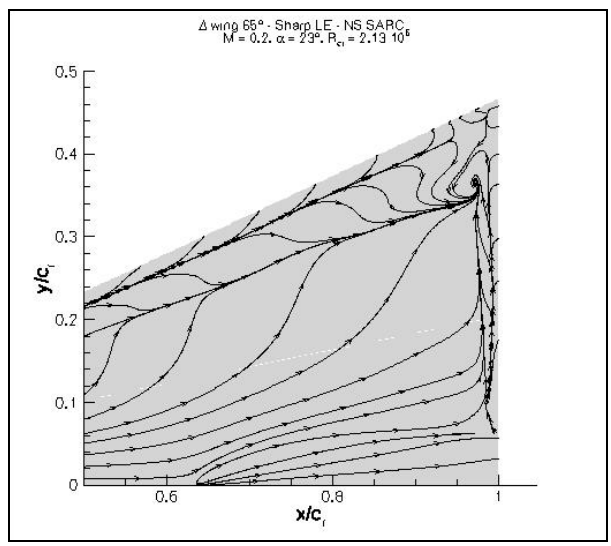

(b) Streamlines

Figure 26-5: Velocity Distribution and Streamlines – Sharp Leading – α = 23° – PG.

The comparison of the results relative to the two grids is presented in Figure 26-6. At this incidence, the pressure distributions are quite similar in space and intensity.

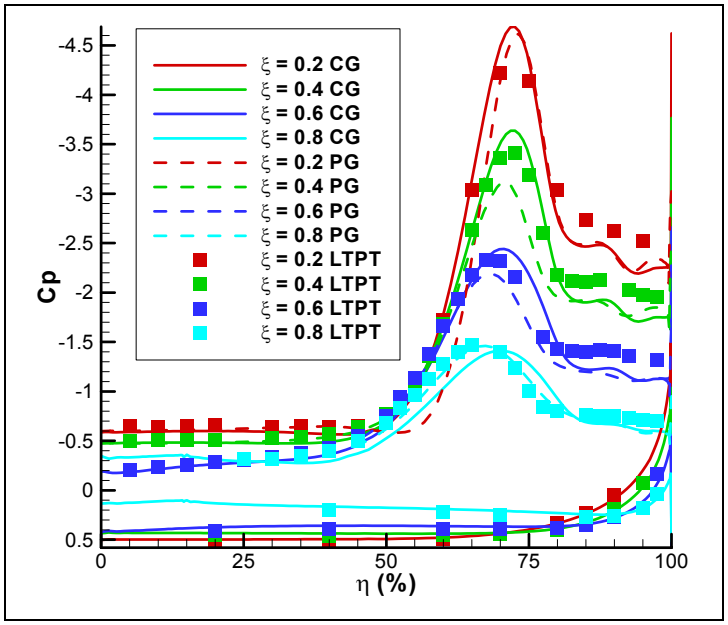

Figure 26-6: Comparison CFD Results / LTPT Data.

A higher incidence has been computed in order to observe the behaviour of the vortex breakdown since its axial displacement is not quite important between 19 and 23°. Figure 26-7 shows the surface pressure distributions at α = 28°. The analysis of the velocity field indicates that the position x/c_r of the vortex breakdown is now lower than 0.5. In these conditions, it is very difficult to predict an accurate position of vortex breakdown when this phenomenon moves in the order of 30 % for a range of 5°. From the experiments conducted in open and closed sections, it has been observed that the sensitivity to the far field conditions must be important for this feature.

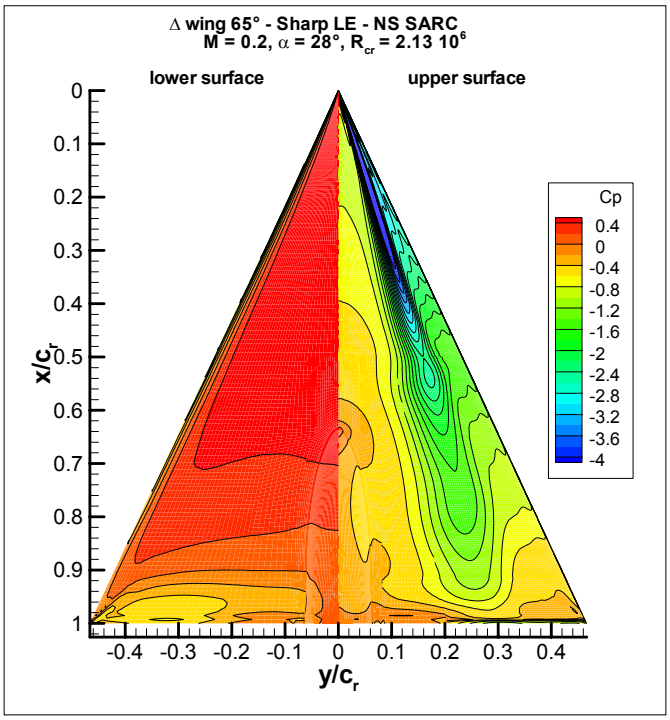

Figure 26-7: Surface Pressure Distribution for the Sharp Leading Edge – PG – α = 28°.

Additional simulations have been carried out at low incidence in order to get further insight to the primary vortex generation mechanism. Most significant results are presented for α = 8°. Figure 26-8 highlights the streamlines in the apex area. As mentioned before, even at very low incidence the flow separates along the leading edge. Although the axial vorticity magnitude is higher in the fore part than in the rear part of the wing, the shear layer is pulled down on the upper surface and generates a unique vortex. Reattachment is observed very close to the leading edge (Figure 26-9 (a)). On and after the second station, the shear layer goes up and supply the primary vortex located further inboard (Figure 26-9 (b), (c) and (d)).

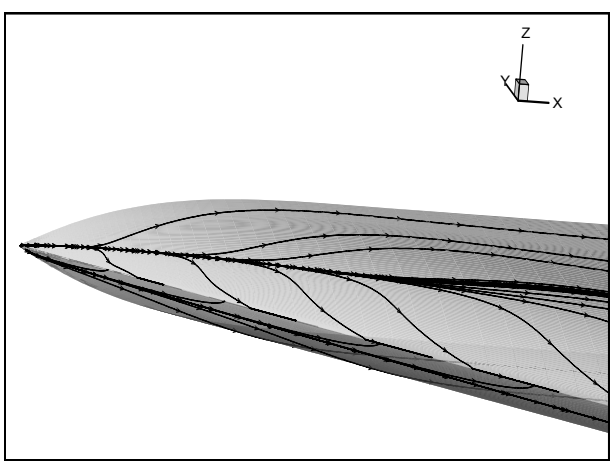

Figure 26-8: Streamline at the Apex of the Sharp Leading Edge – α = 8° – CG.

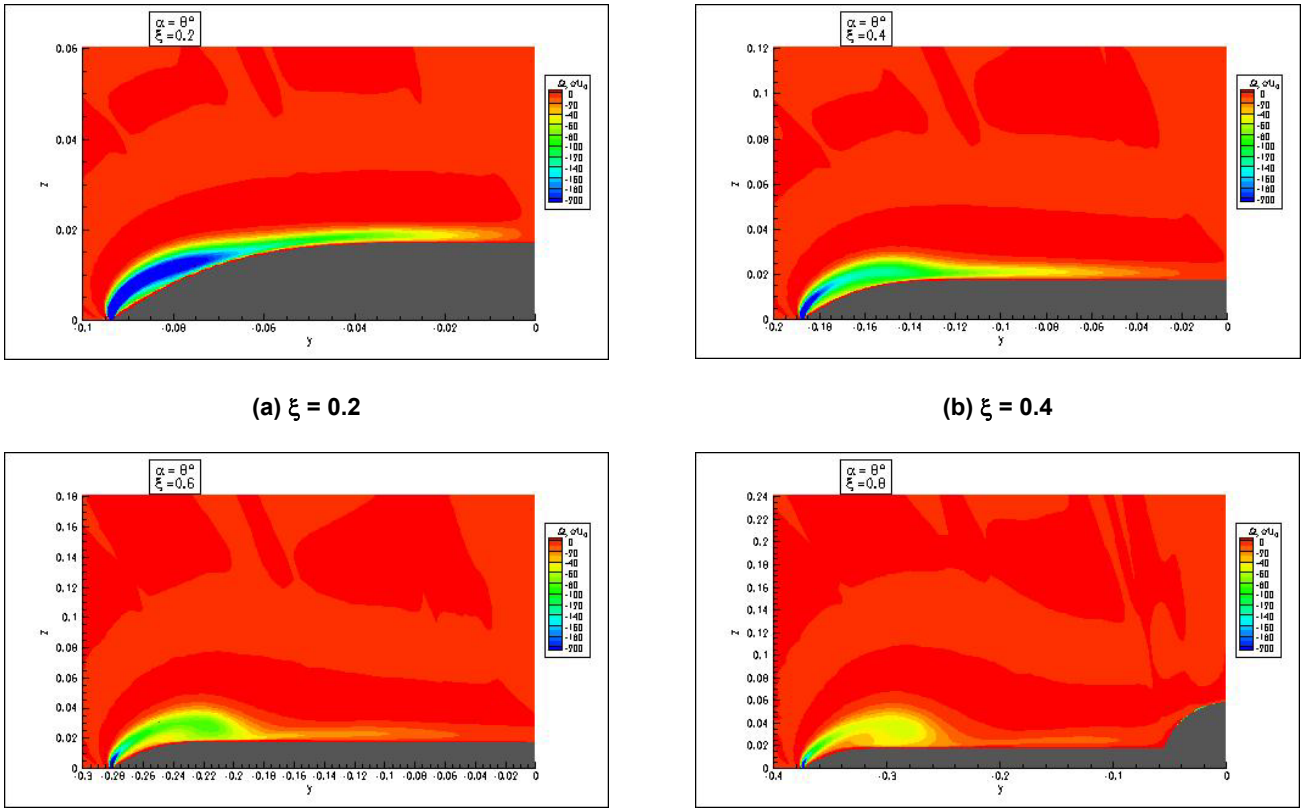

(a) ξ = 0.2

(b) ξ = 0.4

(c) ξ = 0.6

(d) ξ = 0.8

Figure 26-9: Axial Vorticity around the Sharp Leading Edge – CG – α = 8°.

26.3.5 Medium Leading Edge Results

For the 'medium' configuration, the computations are restricted to α = 13, 19 and 23°. As computations carried out with the common grid are relative to higher Mach and Reynolds numbers, no comparison is made between the different grids.

The effect of the turbulence model (SARC and Wilcox k-ω) has been studied in the case of α = 13°. The Figure 26-10 (a) shows the surface pressure distribution. The separation onset takes place at $x/c_r = 0.3$. A comparison of pressure distributions is plotted in Figure 26-10 (b). For this configuration, the SARC model generates a weaker primary vortex than with the k-ω model. The pressure fluctuations located between the primary vortex and the leading edge indicate that a secondary vortex is present at the third and fourth station with the k-ω turbulence model. So, the two equations model is better adapted when the flow is attached on an important part of the wing.

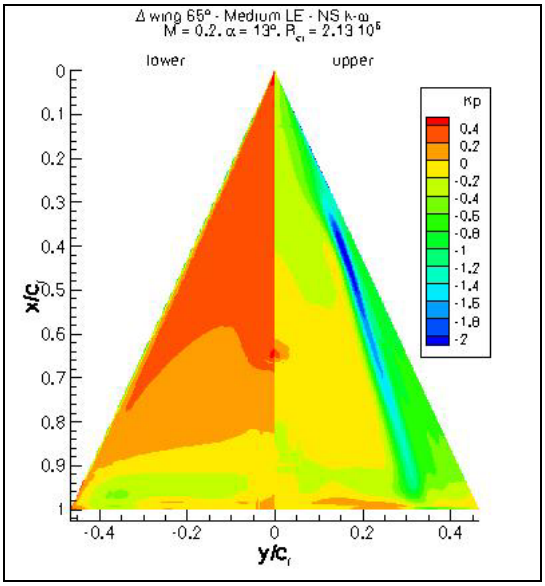

(a) Surface Pressure Distribution

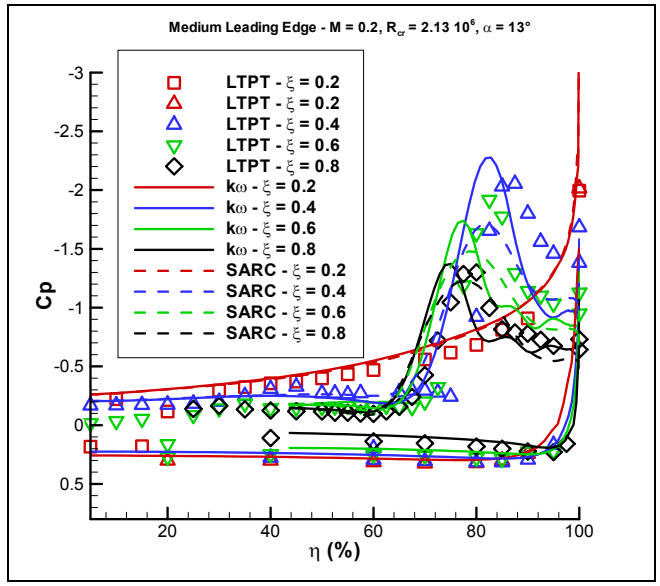

(b) Comparison CFD Results / LTPT Data

Figure 26-10: Effect of Turbulence Model for the Medium Leading Edge – α = 13° – PG.

Within this study, another aerodynamic condition is considered (M = 0.4, R_{cr} = 4 x 10^6) for the same incidence. The surface pressure distributions obtained with the Wilcox k-ω turbulence model fit quite well with Konrath's experiments [26-8] (Figure 26-11 (a) and (b)). This configuration is very interesting for mainly two reasons: the primary vortex appears at mid chord and an inner vortex is observed. As the Mach number increases the flow remains attached on a more important part of the wing. The separation appears at x/c_r = 0.5 at M = 0.4 (Figure 26-11 (b)) against x/c_r = 0.3 at M = 0.2 (Figure 26-10 (a)). A variation of pressure is observed in the central part of the wing for the two configurations. It is more important at M = 0.4 because the inner vortex is confined between the fairing and the primary vortex.

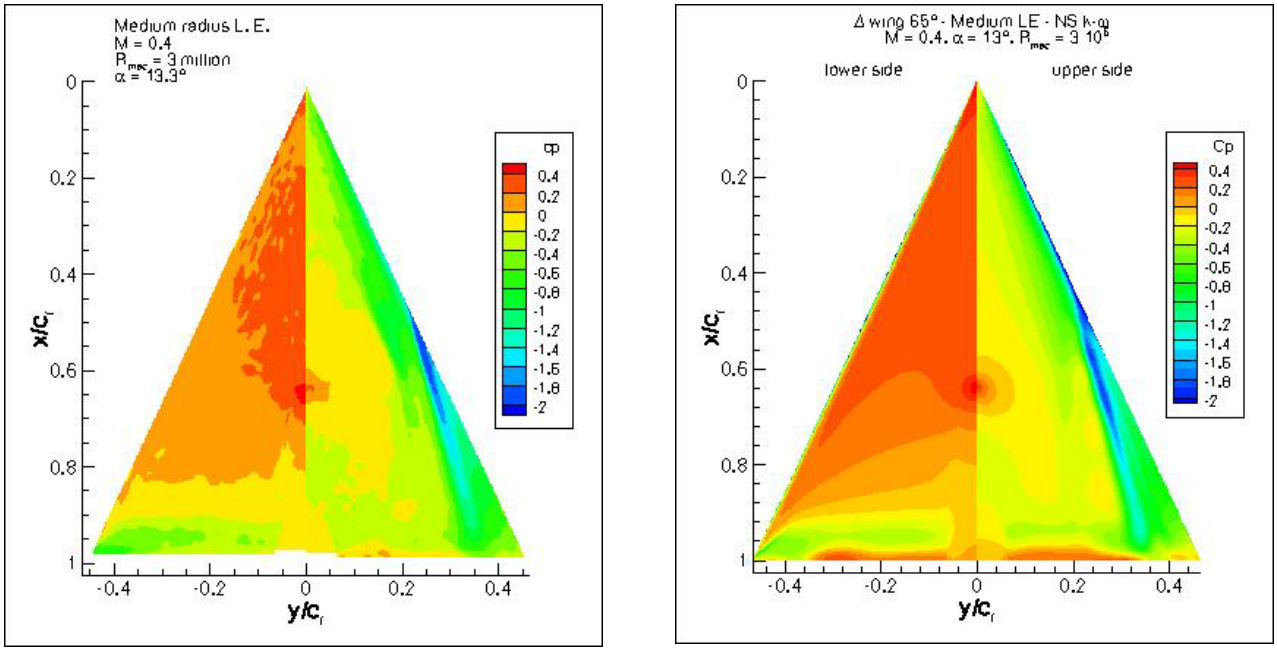

(a) Konrath's Experiment – PSP Measurement **(b) CFD Result – CG**

Figure 26-11: Medium Leading Edge Results – M = 0.4, R_{mac} = 3 x 10^6, α = 13°.

A detailed comparison of pressure distributions is plotted in Figure 26-12. The inner vortex appears earlier in experiment than in computation and the computed inner vortex exhibits a lower intensity. The spatial extensions of the primary vortex are similar but not exactly located at the same place. The difference indicates that the primary vortex appears earlier in the computation.

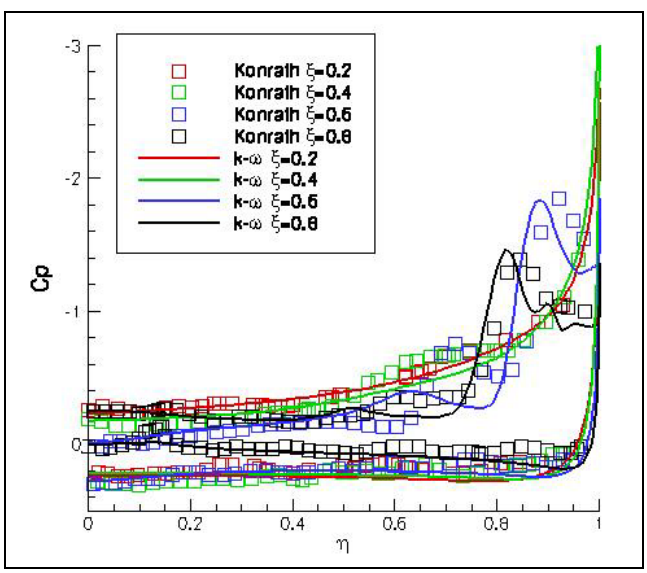

Figure 26-12: Comparison Pressure Distributions – Medium Leading Edge – M = 0.4, R_{mac} = 3 x 10^6, α = 13° – CG.

The Figure 26-13 reveals the topology of the flow by plotting the total pressure loss in different planes above the upper surface. The inner vortex is not very strong but its size is quite large and expands towards the trailing edge. The strong primary vortex starts in the vicinity of mid chord and induces a secondary vortex further downstream.

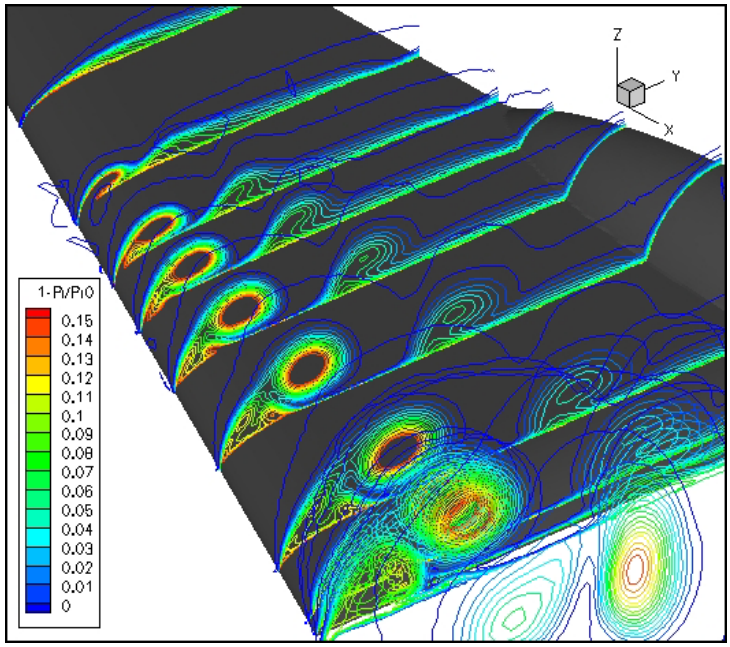

Figure 26-13: Medium Leading Edge Results – M = 0.4, R_{mac} = 3 x 10^6, α = 13° – CG.

For the incidences of 19 and 23°, the SARC turbulence model has been used to compute the solutions since the flow is massively separated. Figure 26-14 shows the surface pressure distribution for the two incidences. The medium leading edge results are quite similar to the sharp leading edge results, excepted in the fore part. Small variations of pressure are observable in the area close to the apex. Figure 26-15 shows the axial vorticity close to the apex for these two incidences. The flow remains attached for x/c_r less than 0.1. The separation moves towards the apex as the incidence increases. The core of the primary vortex is clearly defined and is characterised by high velocity ratio greater than 2. At an incidence of 23° the analysis of the velocity field shows that the primary vortex breakdown appears approximately at the same place for the two leading edges : x/c_r = 0.76 for the medium leading edge against x/c_r = 0.75 for the sharp leading edge. Since the location of the primary vortex is very sensitive to the Mach and Reynolds numbers, the comparison of results when far field conditions are not exactly identical can be misleading.

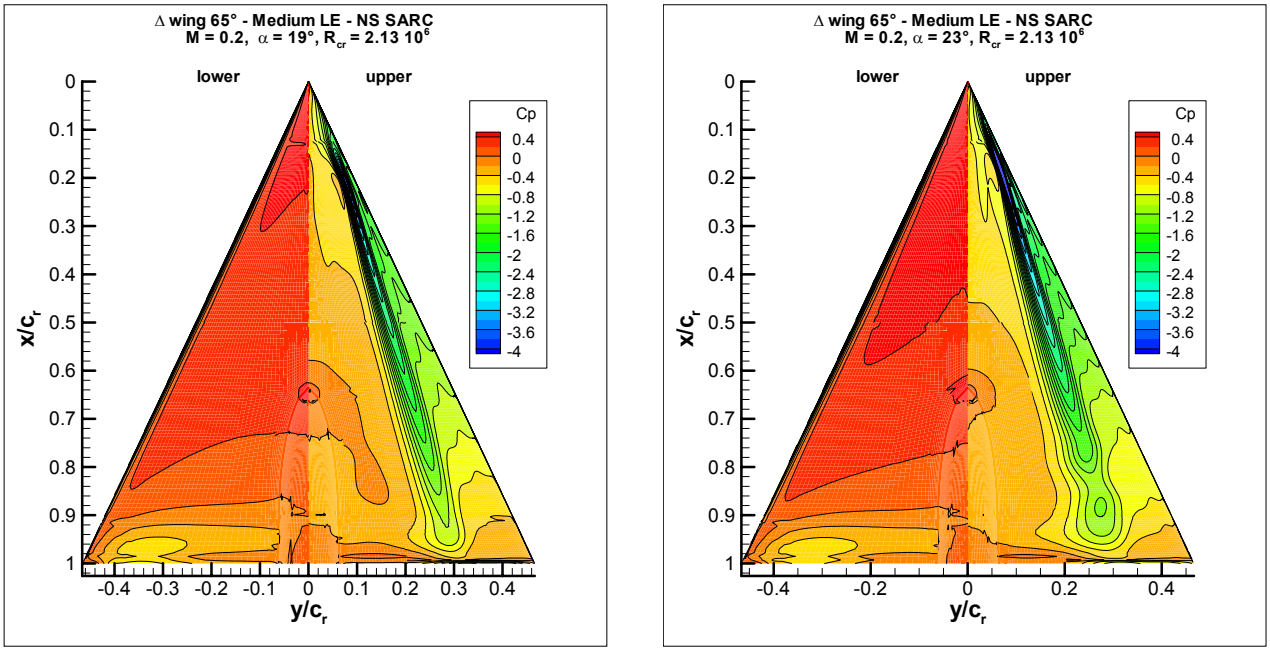

(a) α = 19°

(b) α = 23°

Figure 26-14: Medium Leading Edge – Surface Pressure Distributions – PG.

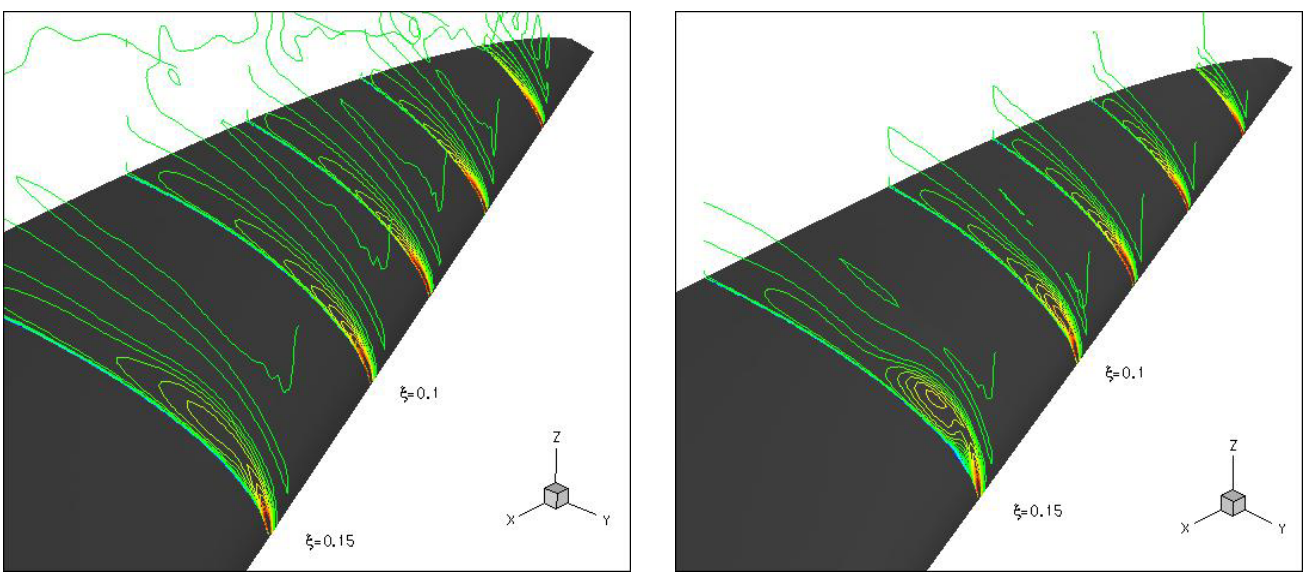

(a) α = 19°

(b) α = 23°

Figure 26-15: Medium Leading Edge Results – Axial Vorticity – PG.

26.4 UNSTEADY APPROACH

In the way to capture the unsteady phenomena present in the rotational flow over slender delta wings, two unsteady computations have been carried out. These computations concern the sharp leading-edge configuration for two different Mach numbers: M = 0.4 and M = 0.8. The Reynolds number based on the mean aerodynamic chord is $R_{mac} = 2 \times 10^6$ and the angle of attack is $\alpha = 25.5°$ for the two computations.

All the computations presented in this section have been performed using the FLU3M solver [26-9], developed by ONERA. This code solves the compressible Navier-Stokes equations on multiblock structured grids. The accuracy of the solver for DNS, LES and hybrid RANS/LES has been assessed in various applications including flows around a two-dimensional airfoil in near stall conditions [26-10], after-body flows [[26-11] – [26-13]], cavity flows [26-14] and synthetic jets in a cross flow [[26-15] – [26-16]].

26.4.1 Computational Method

The second order AUSM scheme [26-17] is used for the discretization of the Euler fluxes. The set of equations is advanced in time using the second-order accurate backward implicit scheme of Gear [26-18]. Moreover, 4 sub-iterations are used in the sub-iterative Newton process and the time step is set equal to 5.0×10^{-7} s.

Hybrid RANS/LES approaches [26-19] represent a credible alternative to RANS and LES computations to improve the description of the rotational flow over slender delta wings at a reasonable cost by taking into account most of the flow unsteadiness. The main idea of these methods is to model the turbulent structures in the attached region of the flow and to solve the large scale structures elsewhere. The global hybrid method used in the current investigation is the EDDES method [26-20], based on the Spalart-Allmaras equation [26-21], which is an evolution of the DDES method [26-22].

The structured grid used in the current study has been generated with the ICEM Hexa meshing tool. The topology is O-H and the number of points is 21×10^6. Moreover, as it is depicted in Figure 26-16, the mesh is locally refined in the region of the rotational flow on the upper surface of the VFE-2 wing.

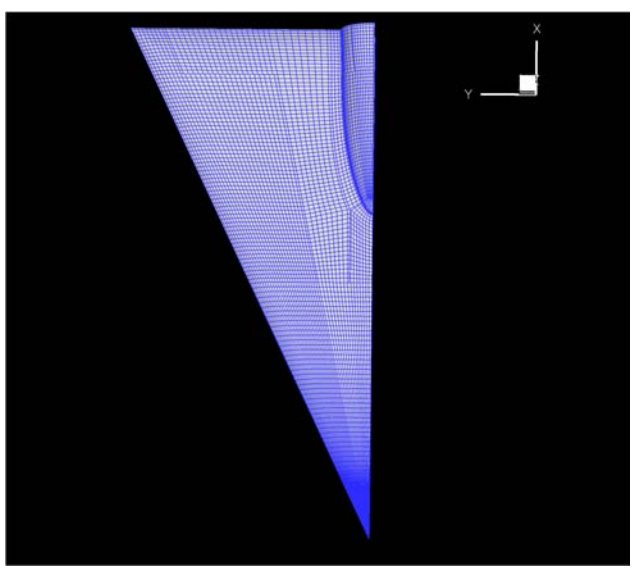

Figure 26-16: Mesh for Unsteady CFD on the Suction Side of the VFE-2 Delta Wing (Only 1 Point Every 4).

26.4.2 Study of the Instantaneous Flow

The aim of this section is to present the instantaneous flow developing over the sharp leading edge configuration for the two Mach numbers. The turbulent structures can be educed by plotting an iso-surface of the Q criterion defined as follows [26-23]:

$$Q = -\frac{1}{2}(S_{ij}S_{ij} - \Omega_{ij}\Omega_{ij})$$

where S and Ω denote respectively the strain and rotation tensors.

This is a useful quantity to highlight the flow regions where the turbulence is resolved. Thus, an iso-surface of $Q = 1000 \times \frac{c}{U_\infty}$ flooded by the non-dimensional longitudinal velocity $\frac{u}{U_\infty}$ is shown in Figure 26-17 for the two considered Mach numbers.

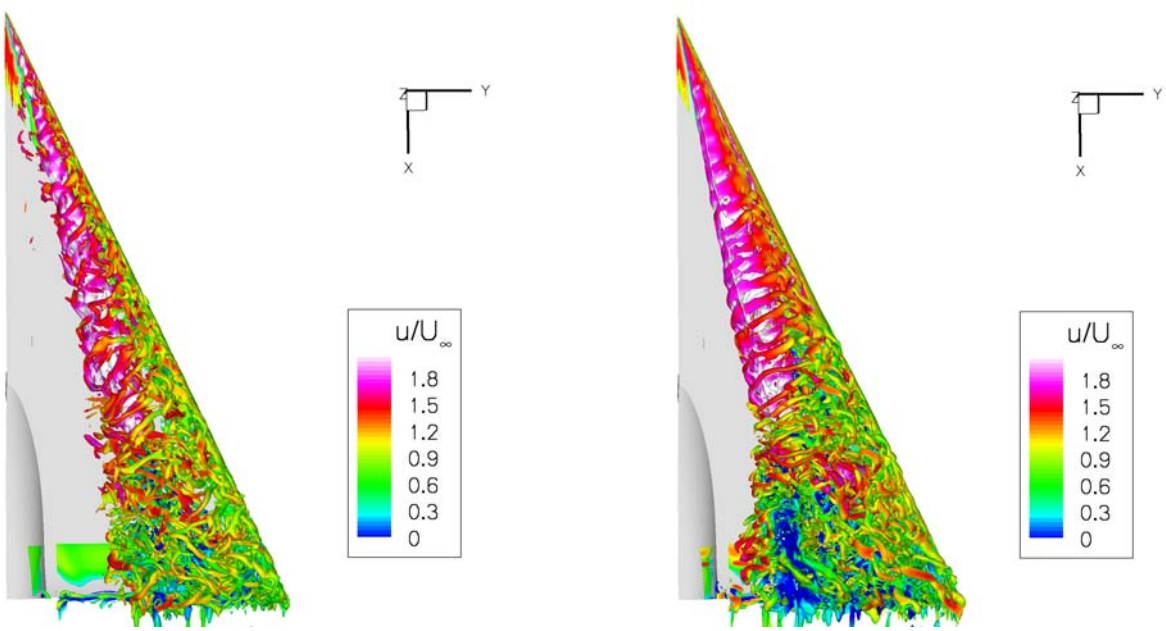

Figure 26-17: Representation of the Flow Unsteadiness (Left: M = 0.4; Right: M = 0.8).

Similarities in the two flows clearly appear in this figure. One can observe the formation of the leading-edge vortex, denoted by the intense acceleration of the longitudinal flow. This vortex undergoes an abrupt disorganisation, known as vortex breakdown and which is identified by a sudden appearance of a stagnation flow (appearing in blue in this figure). Moreover, small-scale structures (in comparison with the length-scale of the leading-edge vortex) are visible in the shear layer emanating from the leading-edge all around the vortex. These structures are identified as being the Kelvin-Helmholtz structures.

Both flows exhibit some differences. The first one is the shape of the leading-edge vortex, which is flatter and more extended in the M = 0.8 case than in the other case. Moreover, the reverse flow, consequence of the vortex breakdown is more extended and inboard in the transonic case than in the subsonic one. These observations will be pursued in the study of the time-averaged flow.

26.4.3 Study of the Time-Averaged Flow

The two computations have been time-averaged on a period of 5 T_c, where T_c is the time-scale defined by $T_c = \frac{c}{U_\infty}$. It represents a duration equals to 9.8 ms for the transonic case and 19.6 ms for the subsonic one.

The distributions of the pressure coefficient C_p on the suction side of the VFE-2 delta wing for the two computational cases are represented in Figure 26-18 and are compared to the experimental data.

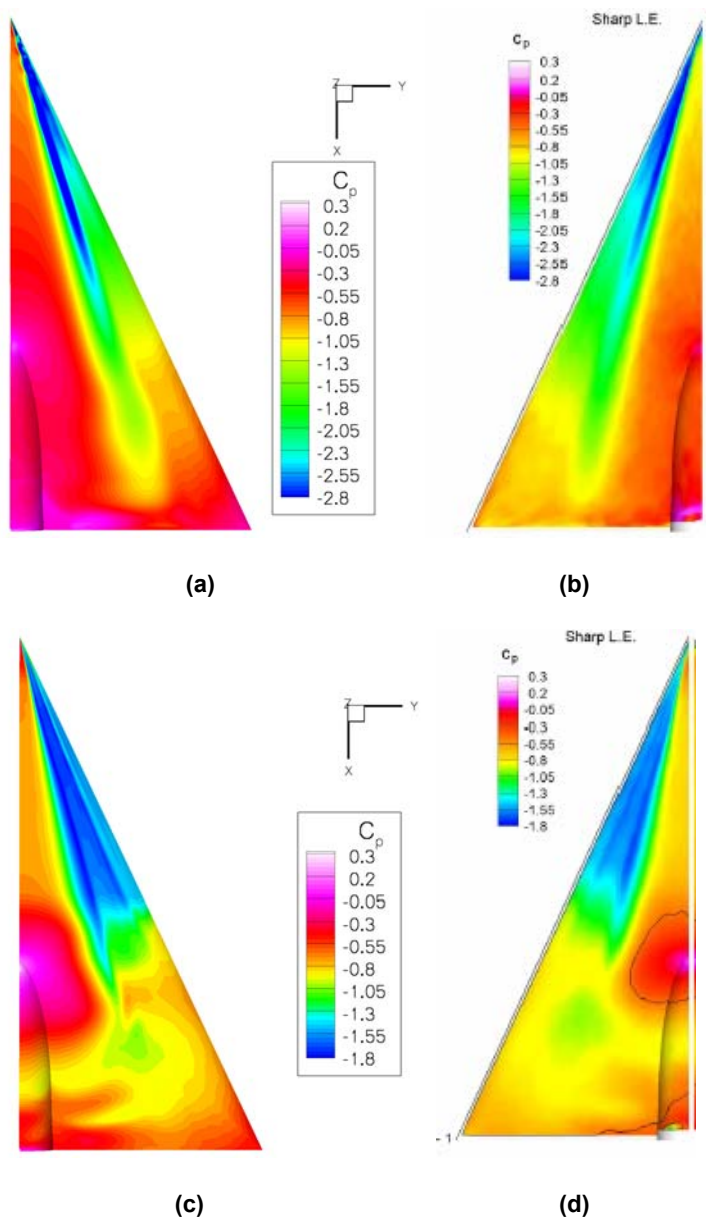

Figure 26-18: Distribution of C_p on the Suction Side for the M = 0.4 Case ((a): Numerical; (b): Exp.) and M = 0.8 Case ((c): Numerical; (d): Exp.).

As depicted in this figure, a very good agreement with the experimental PSP data of Konrath et al [26-8] is obtained for the two computations. Note that the color map is not quite identical between the experimental and numerical representations but the levels of C_p are quite identical. For the subsonic case, a large low-pressure area is predicted on the suction side, this region being the foot print of the leading-edge vortex. The distribution of C_p is somewhat different for the transonic case. In fact, the first observation which can be made is that the low-pressure peak is much weaker in this case than in the previous one. Moreover, the foot print of the leading-edge vortex is more inboard and a second low-pressure peak is observed between the one associated to the primary vortex and the leading-edge. Furthermore, an increase of the Mach number leads to a shortening of the depression. In fact, only a small region of low C_p is present in the last half part of the delta wing.

In order to understand these observations, Figure 26-19 shows contours of $\frac{u}{U_\infty}$ in several planes perpendicular to the surface of the VFE-2 delta wing.

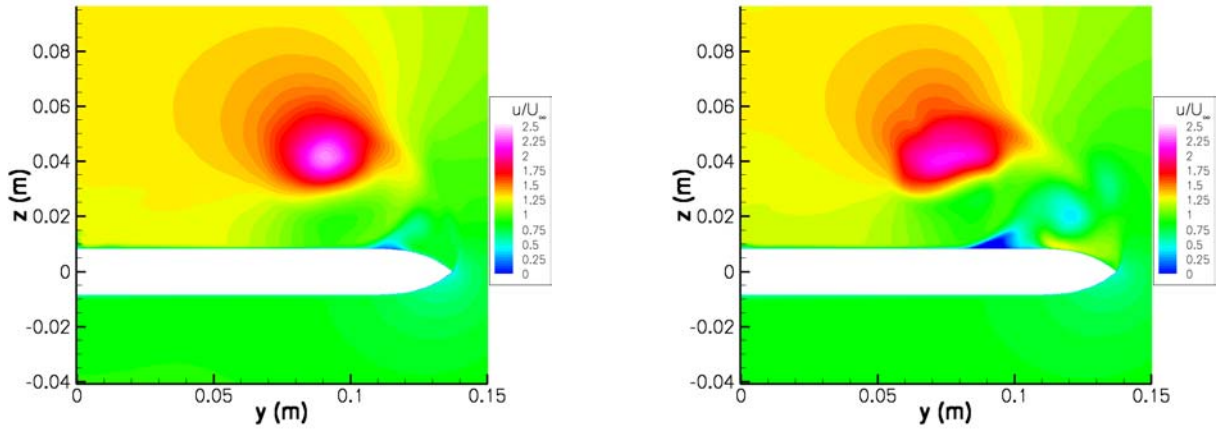

$x/c_r = 0.6$

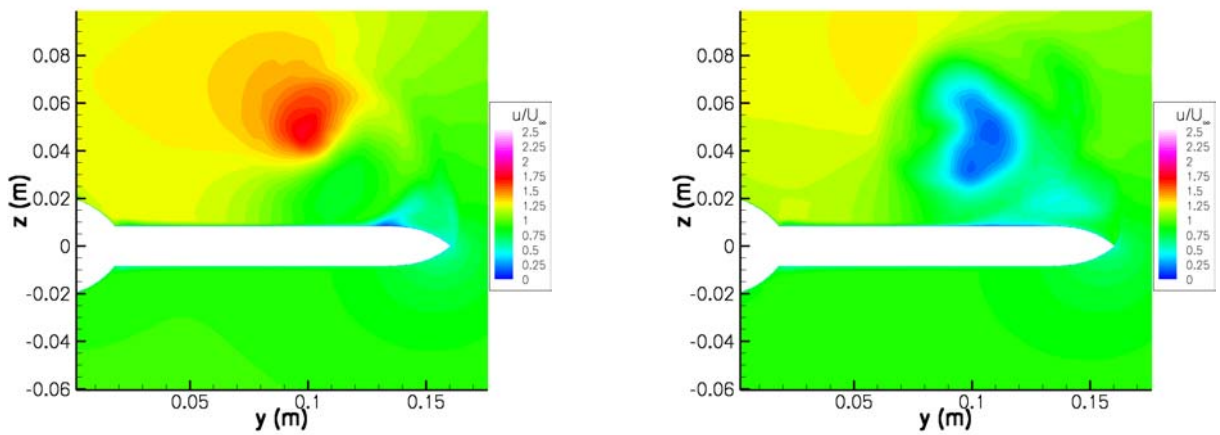

$x/c_r = 0.7$

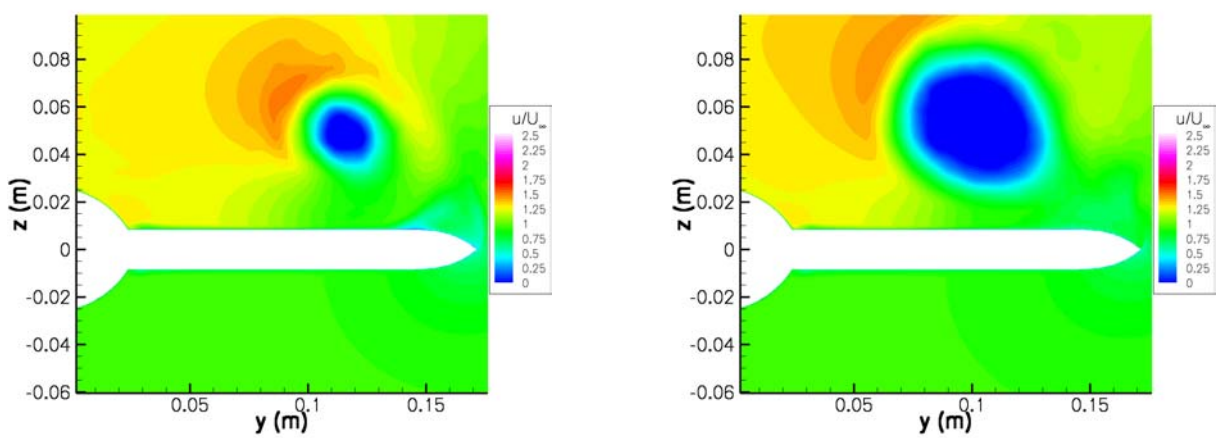

$x/c_r = 0.75$

Figure 26-19: Evolution of the Longitudinal Velocity in Several Planes Perpendicular to the Surface of the Wing (Left: M = 0.4; Right: M = 0.8).

The observation of the longitudinal velocity at $x/c_r = 0.6$ confirms that an increase of the Mach number leads to a modification of the shape of the leading-edge vortex. In the transonic case, the vortex is flatter and nearer to the surface of the wing than in the subsonic case. These observations are in agreement with experimental results of Squire [26-24] and Erickson [26-25]. Moreover, the acceleration of the longitudinal flow in the vortex core is more important in the subsonic case ($\frac{u}{U_\infty}$ reaches 2.5) than in the transonic one, where the maximum of the non-dimensional velocity equals to 2.2 (resulting in a local Mach number equals to 1.96). Another important feature of the flow in the M = 0.8 case at $x/c_r = 0.6$ is the intense second separation just outboard of the primary vortex. This is caused by the embedded cross-shock waves which occur between the primary vortex and the surface of the delta wing [26-26]. This second separation is the cause of the second low-pressure peak observed in the previous figure. Moreover, it appears that the vortex breakdown occurs earlier in the transonic case as it is illustrated by the reverse flow at $x/c_r = 0.7$. Note that this time-averaged position is in a good agreement with stereo-PIV observations of Schröder et al [26-27]. Parallel to this observation, a strong leading-edge vortex is still present at this position for M = 0.4. The vortex breakdown occurs further downstream, as it is illustrated by the reverse flow at $x/c_r = 0.75$. Furthermore, one can observe at this position the acceleration of the flow between the sting and the region of reverse flow. In fact, the non-dimensional velocity reaches 1.5 in the two cases, resulting in a supersonic flow (M = 1.1) in the M = 0.8 case.

The transonic flow over delta wing is the place of several shocks waves. The interactions between the shock waves and the primary vortex could explain the difference in the time-averaged vortex-breakdown localization. The acceleration of the flow and the variation of the section beneath the primary vortex induce the formation of shocks (see Figure 26-20), the previously evocated cross-flow shocks waves. But some shock waves are also observed in the region of the trailing edge, the rear/terminating shock waves.

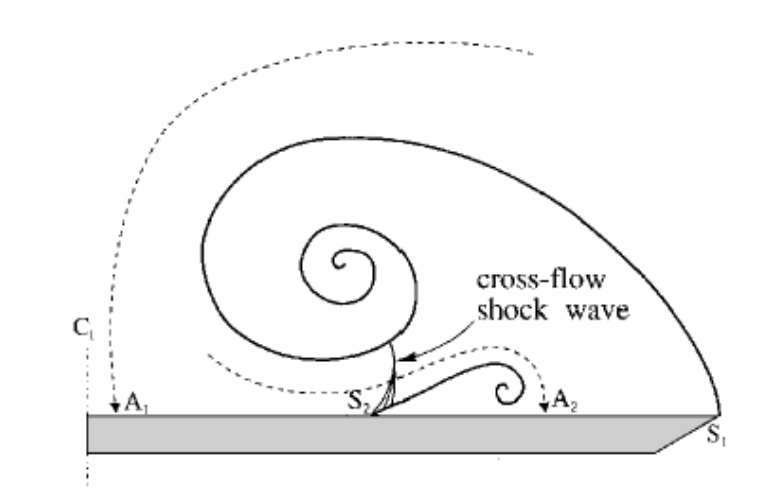

Figure 26-20: Representation of the Cross-Flow Shock Waves (from [26-26]).

The Figure 26-21 presents an isosurface of $Q = 400 \times \frac{c}{U_\infty}$ in the time-averaged flow flooded by C_p and numerical schlieren-like visualization (isocontours of $\|grad(\rho\|$) in the symmetry plane.

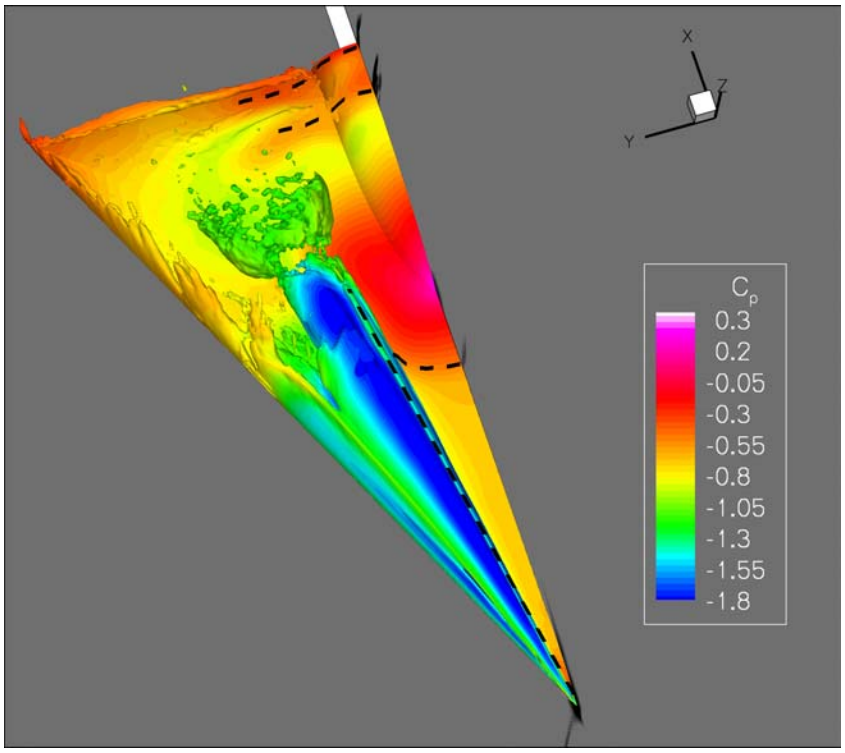

Figure 26-21: Representation of Time-Averaged Flow in the M = 0.8 Case (the dashed-lines represent the shocks).

This figure highlights the existence of three shocks in the symmetry plane. The first one is located just upstream of the sting (x/c_r = 0.54) and is curved in the longitudinal direction (see the shape of the black dashed-line). The occurrence of this shock is imputable to the slowing down of the flow induced by the presence of the sting. Two other shocks are visible, just upstream of the trailing-edge of the delta wing. The one located at x/c_r = 0.98 ensures the natural balance of the upper and lower surface pressures. The presence of the shock at x/c_r = 0.92 may be caused by the progressive slowing down of the supersonic flow between the sting and the reverse flow downstream from the time-averaged position of the vortex breakdown. The presence of two rear shocks had been underlined in experimental investigations of the transonic flow over delta wings of Elsenaar and Hoeijmakers [26-28] and Houtman and Bannink [26-29].

The interaction of these shocks with the leading-edge vortex can cause a premature vortex-breakdown, in comparison with the subsonic case, as suggested by experimental observations by Donohoe et al [26-26] and Kandil et al [26-30]).

26.4.4 Spectral Analysis

One interest of hybrid RANS/LES methods in comparison with classical RANS computations is the access to the unsteadiness of the flow, as it was suggested in the presentation of the instantaneous flow.

To accomplish this spectral analysis, the temporal evolution of the longitudinal velocity is analysed at two different positions: the first one (probe P_1) in the leading-edge vortex core and the second one (probe P_2) in the reverse flow downstream from the mean vortex-breakdown location (see Figure 26-22).

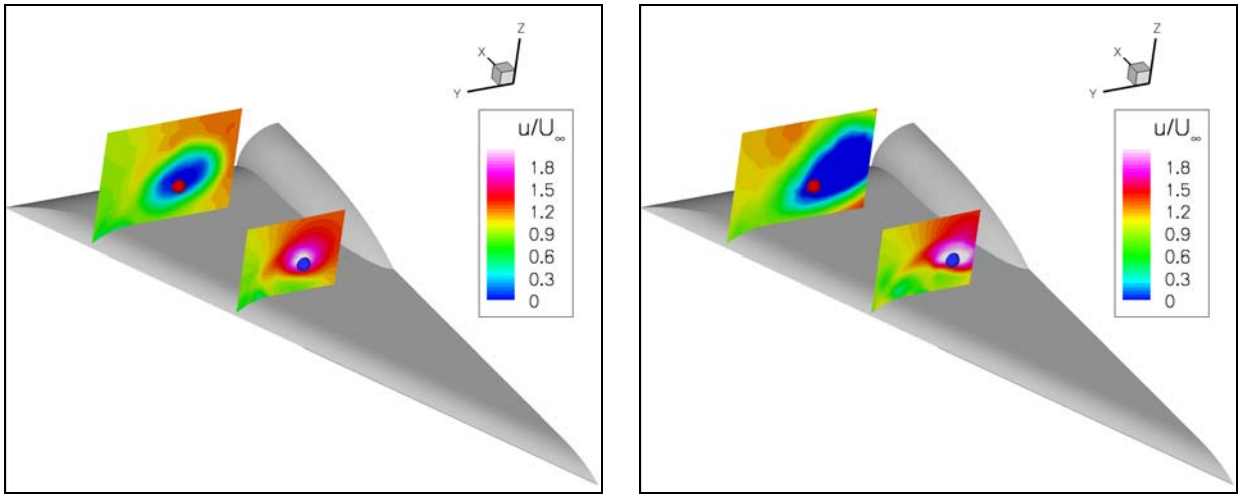

Figure 26-22: Positions of the Two Probes P_1 and P_2 Relatively to the Time-Averaged Flow (Left: M = 0.4; Right: M = 0.8).

The spectral analysis of these signals has been performed using the method of Burg [26-31] and the Power Spectral Density (PSD) is represented in Figure 26-23.

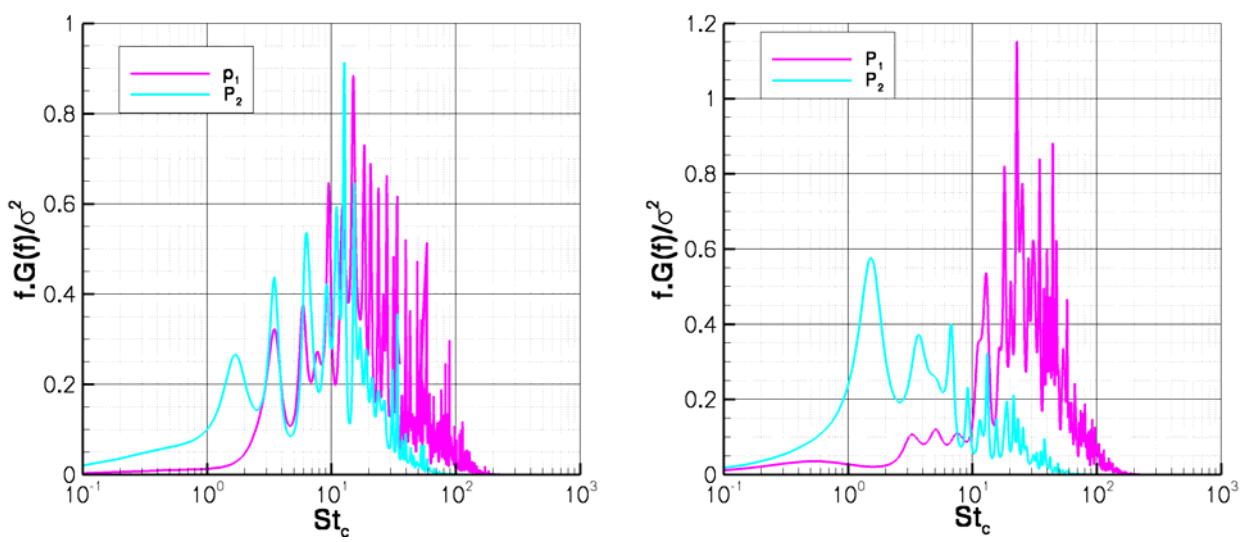

Figure 26-23: PSD of the Non-Dimensional Longitudinal Velocity at P_1 and P_2 (Left: M = 0.4; Right: M = 0.8).

The first observation which can be made is that the two signals exhibit a dominant frequency at the first probe location P_1. This frequency corresponds to St_c = 16 in the M = 0.4 case and St_c = 22 in the transonic case. Moreover, two peaks at St_c = 3 and St_c = 5 are also present at this position. These frequencies are usually observed in experimental [[26-32] – [26-33]] and numerical [26-34] investigations and are associated to the Kelvin-Helmholtz instability in the shear layer emanating from the leading-edge.

The PSD at the probe P_2 is somewhat different of the previous one. In fact, a dominant frequency at Stc ≈ 10 is still present in the subsonic case but high-frequency is no more discernable in the transonic case. In spite of this, the two PSD present some similarities. An increase of the amplitude of the peaks at $St_c = 3$ and $St_c = 5$ is observed. Moreover, a new peak appears in the two signals at the non-dimensional frequency Stc = 1.6. Once again, this non-dimensional frequency is experimentally [[26-35] – [26-36]] and numerically [26-37] observed downstream from the vortex breakdown location and is associated with the helical mode instability.

26.5 CONCLUSIONS

The flow over a delta wing equipped with a sharp leading edge at high angle of attack is exceedingly complex, including separated flow, high streamwise curvature and large pressure gradient. Viscosity promotes a secondary vortex and influences the location of the vortex breakdown which is difficult to calculate. In the case of the rounded leading edge the flow can remain attached on an important part of the wing and the separation line is not fixed by the leading edge.

The phenomenon of vortex breakdown observed at high angle of attack can be merely predicted by Euler simulations. The introduction of viscosity is needed to simulate the secondary vortex and its interaction with the primary one. The choice of an adapted turbulence model is important to capture some aspect of the flow especially when the flow remains attached on the fore part of the wing. Since the results of simulations are in relatively good agreement with experimental data for these aerodynamic conditions (low Mach and Reynolds number) steady RANS approach with sufficiently refined grids is sufficient to predict the main features of the flow and determine the general tendency of Reynolds and Mach number effects.

However, this approach reveals several discrepancies with respect to experimental results: location of the vortex breakdown at high incidence due to an under-prediction of longitudinal and streamwise velocity in the vortex core and the secondary vortex is under-estimated. For the case with rounded leading edge, the onset of the primary leading edge separation is shifted upstream in comparison with the experimental data.

The EDDES computations allow the study of the effect of the compressibility on the vortical flow over the sharp leading-edge wing. As it has been presented, the flow over the VFE-2 delta wing in the M = 0.4 and M = 0.8 ($\alpha = 25.5°$) cases exhibits some common characteristics. In fact, the formation of the primary vortex and the occurrence of its breakdown are observed in the two computations. Moreover, the spectral analysis reveals the existence of the Kelvin-Helmholtz instability in the region of the vortex core and the existence of the helical instability downstream from the time-averaged location of the vortex breakdown in the two computations. In spite of these similarities, these two computations highlight the effect of an increase of the Mach number on the vortical flow which develops over delta wings. In fact, several shocks occur in the M = 0.8 case. Cross-flow shocks lead to the separation of the boundary layer beneath the leading-edge vortex and then induce the second vortex. The presence of three shocks perpendicular to the surface of the VFE-2 delta wing and to the longitudinal direction may cause the premature vortex-breakdown in comparison with the subsonic case.

26.6 REFERENCES

[26-1] Rediniotis, O.K., Stapountzis, H. and Telionis, D.P.: *Periodic Vortex Shedding over Delta Wing*, AIAA Journal, Vol. 31, No. 9, September 1993, pp. 1555-1561.

[26-2] Menke, M., Yang, H. and Gursul, I.: *Experiments on the Unsteady Nature of Vortex Breakdown Over Delta Wings*, Exp. Fluids, Vol. 27, No. 3, 1999, pp. 262-272.

[26-3] Cambier, L. and Gazaix, M.: *elsA: An efficient Object-Oriented Solution to CFD Complexity*, 40th AIAA Aerospace Science Meeting and Exhibit, Reno (USA), January 14-17, 2002.

[26-4] Cambier, L. and Veuillot, J.: *Status of elsA Software for Flow Simulation and Multidisciplinary Applications*, 46th AIAA Aerospace Science Meeting and Exhibit, Reno (USA), January 7-11, 2008.

[26-5] Fritz, W.: *VFE-2 Delta Wing Structured Grids*, EADS-M Technical Note.

[26-6] Chu, J. and Luckring, J.M.: *Experimental Surface Pressure Data Obtained on 65° Delta Wing Across Reynolds Number and Mach Number Ranges*, NASA Technical Memorandum 4645, Langley Research Center, Hampton, Virginia, February 1996.

[26-7] Le Roy, J.-F., Rodriguez, O. and Kurun, S.: *Experimental and CFD Contribution to Delta Wing Vertical Flow Understanding*, 46th AIAA Aerospace Science Meeting and Exhibit, Reno (USA), January 7-11, 2008.

[26-8] Konrath, R., Klein, C., Engler, R. and Otter, D.: *Analysis of PSP Results Obtained for the VFE-2 65° Delta Wing Configuration at Sub- and Transonic Speeds*, 44th AIAA Aerospace Science Meeting and Exhibit. Reno (USA), January 9-12, 2006.

[26-9] Pechier, M.: *Prévisions numériques de l'effet Magnus pour des configurations de munition*, PhD Thesis, 1999.

[26-10] Mary, I. and Sagaut, P.: *Large Eddy Simulation of the Flow around an Airfoil Near Stall*, AIAA Journal, Vol. 40, No. 6, pp. 1139-1146, 2002.

[26-11] Deck, S., Garnier, E. and Guillen, P.: *Turbulence Modelling Applied to Space Launcher Configurations,* Journal of Turbulence, Vol. 3, No. 1, 2002.

[26-12] Deck, S. and Thorigny, P.: U*nsteadiness of an Axisymmetric Separating-Reattaching Flow: Numerical Investigation*, Physics of Fluids, Vol. 19, 2007.

[26-13] Simon, F., Deck, S., Guillen, P., Sagaut, P. and Merlen, A.: *Numerical Simulation of the Compressible Mixing Layer Past an Axisymmetric Trailing Edge*, Journal of Fluid Mechanics, Vol. 591, pp. 215-253, 2007.

[26-14] Larchevêque, L., Labbé, O., Mary, I. and Sagaut, P.: *LES of a Compressible Flow Past a Deep Cavity*, Physics of Fluids, Vol. 14, 2003.

[26-15] Dandois, J., Garnier, E. and Sagaut, P.: *Unsteady Simulation of Synthetic Jet in a Crossflow*, AIAA Journal, Vol. 44, No. 2, pp. 225-238, 2006.

[26-16] Dandois, J., Garnier, E. and Sagaut, P.: *DNS/LES of Active Separation Control*, Journal of Fluid Mechanics, Vol. 574, pp. 25-58, 2007.

[26-17] Mary, I.: *Méthode de Newton approchée pour le calcul d'écoulements instationnaires comportant des zones à très faible nombre de Mach*, PhD Thesis, 1999.

[26-18] Gear, C.W.: *Algorithm 407-DIFSUB for the Solution of Ordinary Differential Equations*, Commun. ACM, Vol. 14, No. 3, pp. 185-190, 1971.

[26-19] Sagaut, P., Deck, S. and Terracol, M.: *Multiscale and Multiresolution Approaches in Turbulence*, Imperial College Press, 2006.

[26-20] Riou, J., Garnier, E., Deck, S. and Basdevant, C.: *An Extension of DDES Applied to the Computation of a Generic Missile Fin in Transonic Regime*, ERCOFTAC-ETMM7, N95, 2008.

[26-21] Spalart, P.R. and Allmaras, S.R.: *A One-Equation Turbulence Model for Aerodynamic Flows*, AIAA Paper 1992-04339, 1992.

[26-22] Spalart, P.R., Jou, W.H., Strelets, M. and Allmaras, S.R.: *Comments on the Feasibility of LES for Wings, and on a Hybrid RANS/LES Approach*, In Proceedings pp. 137-147, 1st AFSOR Int. Conf. on DNS/LES Ruston, 1998.

[26-23] Jeong, J. and Hussain, F.: *On the Identification of a Vortex,* Journal of Fluid Mechanics, Vol. 285, pp. 69-94, 1995.

[26-24] Squire, L.C.: *Leading-Edge Separations and Cross-Flow Shocks on Delta Wings*, AIAA Journal, Vol. 23, No. 3, pp. 312-325, 1985.

[26-25] Erickson, G.E.: *Experimental Study of the Vortex Flow Behaviour on a Generic Fighter Wing at Subsonic and Transonic Speeds*, AIAA Paper 87-1262, 1987.

[26-26] Donohoe, S.R. and Bannink, W.J.: *Surface Reflective Visualisations of Shock-Wave/Vortex Interactions Above a Delta Wing*, AIAA Journal, Vol. 35, No. 10, pp. 1568-1573, 1997.

[26-27] Schröder, A., Agocs, J., Frahnert, H., Otter, D., Mattner, H., Kompenhans, J. and Konrath, R.: *Application of Stereo PIV to the VFE-2 65° Delta Wing Configuration at Sub- and Transonic Speeds*, AIAA Paper 2006-3486, 2006.

[26-28] Elsenaar, A. and Hoeijmakers, H.W.M.: *An Experimental Study of the Flow over a Sharp-Edged Delta Wing at Subsonic and Transonic Speeds*, AGARD Conference Proceedings Vortex Flow Aerodynamics, pp. 15.1-15.19, AGARD-CP-494, 1991.

[26-29] Houtman, E.M and Bannink, B.J.: *Experimental and Numerical Investigation of the Vortex Flow over a Delta Wing at Transonic Speed*, AGARD Conference Proceedings Vortex Flow Aerodynamics, pp. 5.1-5.11, AGARD-CP-494, 1991.

[26-30] Kandil, O.A., Kandil, H.A. and Liu, C.H.: *Shock-Vortex Interaction Over a 65-degree Delta Wing in Transonic Flow*, AIAA Paper 93-2973, 1993.

[26-31] Burg, J.P.: *Maximum Entropy Spectral Analysis*, Modern Spectrum Analysis, D.G. Childers, pp. 34-41, IEEE Press, 1978.

[26-32] Gad-El-Hak, M. and Blackwelder, R.F.: *The Discrete Vortices from a Delta Wing*, AIAA Journal, Vol. 23, No. 6, pp. 961-962, 1985.

[26-33] Lowson, M.V.: *The Three Dimensional Vortex Sheet Structures on Delta Wings*, In Fluid Dynamics of Three Dimensional Turbulent Shear Flows and Transition, pp. 11.1-11.16, AGARD-CP-438, 1988.

[26-34] Gordnier, R.E. and Visbal, M.: *Compact Difference Scheme Applied to the Simulation of a Low Sweep Delta Wing Flow*, AIAA Journal, Vol. 43, No. 8, pp. 1744-1752, 2005.

[26-35] Furman, A. and Breitsamter, C.: *Investigation of Flow Phenomena on Generic Delta Wing*, ICAS, 2006.

[26-36] Lambert, C. and Gursul, I.: *Insensitivity of Unsteady Vortex Interactions to Reynolds Number*, AIAA Journal, Vol. 38, No. 5, pp. 937-939, 2000.

[26-37] Görtz, S.: *Time Accurate Euler Simulations of a Full Span Delta Wing at High Incidence*, AIAA Paper 2003-4304, 2003.